Aerodynamic shape optimisation, wind tunnel measurements and CFD analysis of a MAV wing

M. R. A. Nabawy
mostafa.ahmednabawy@postgrad.manchester.ac.uk
School of Mechanical, Aerospace and Civil Engineering
The University of Manchester
Manchester, UK
Aerospace Engineering Department, Cairo University
Giza, Egypt

M. M. ElNomrossy
Production, Energy and Automatic Control Department
French University
Cairo, Egypt

M. M. Abdelrahman
G. M. ElBayoumi
Aerospace Engineering Department, Cairo University
Giza, Egypt

ABSTRACT

The aerodynamic shape optimisation of a micro air vehicle (MAV) wing is performed to obtain the basic wing geometrical characteristics which produce the maximum range and endurance requirements. Multhopp's method based on Prandtl's classical lifting line theory is used for the determination of the spanwise load distribution required during the optimisation process. The obtained lift and drag characteristics are used for the derivation of the range and endurance equations of an electrically driven micro air vehicle. The optimisation process is based on the modified feasible directions gradient based optimisation algorithm. Results are validated using wind tunnel measurements showing very good agreement. Results are also compared with solutions to the Navier-Stokes equations obtained with ANSYS-CFX finite elements using different turbulence models. These include the k-ε and the shear stress transport (SST) models as well as the Reynolds stress model.

Paper No. 3728. Manuscript received 3 June 2011, revised version received 1 December 2011, accepted 3 March 2012.
https://doi.org/10.1017/S000192400000717X Published online by Cambridge University Press

NOMENCLATURE

a_o	aerofoil lift curve slope (radian^{-1})
AR	aspect ratio
b	span (m)
c	local chord (m)
c_l	local lift coefficient
c_r	root chord (m)
c_t	tip chord (m)
C_L	lift coefficient
C_D	drag coefficient
C_{Di}	induced drag coefficient
D	drag force (N)
E	air vehicle endurance (seconds)
i	incidence angle (radians)
I	electric current (Ampere)
L	lift force (N)
m	number of wing stations solved
n	signifies vortex location
N	sample size
P	brake power (Watt)
P_A	available power (Watt)
P_x	precision uncertainty of sample x
Q_f	final amount of electric charge stored in battery
Q_i	initial amount of electric charge stored in battery
R	air vehicle range (m)
s	distance (m)
S	planform area (m^2)
S_x	sample standard deviation
t	time (seconds)
$t_{\alpha/2,N-1}$	student t-distribution
TR	taper ratio
U	free stream velocity (m/sec.)
V	battery's voltage (Volt)
w_i	induced downwash velocity (m/sec.)
W	air vehicle weight (N)
y	wing spanwise station at which the downwash velocity is desired (m)
y'	location of the vortices causing the downwash (m)

Greek symbols

α	wing geometric angle-of-attack (radians)
α_e	wing effective angle-of-attack (radians)
α_i	wing induced angle-of-attack (radians)
ε	downwash angle (radians)
ε_o	downwash angle at zero angle-of-attack (radians)
γ	non-dimensional spanwise circulation strength distribution

https://doi.org/10.1017/S000192400000717X Published online by Cambridge University Press

Γ	spanwise circulation strength distribution
η	installed propeller efficiency
λ	wing local aspect ratio
ν	particular span station where the downwash is to be found
ρ	air density (Kg/m^3)
ζ	spanwise station where vortices are located

Subscripts

ht	horizontal tail
max	maximum
MAV	micro air vehicle
w	wing

1.0 INTRODUCTION

MAVs have gained great attention and have been a subject of considerable interest by the aeronautical community over the last several years. Their development, design, analysis, and modelling including shape, aerodynamics, structures and control aspects have always presented a big challenge. However, many unique designs have been designed, built and flown recently[1-4]. MAVs should work in places and situations where larger vehicles could not exit including both military and civilian sectors. They are also considered an ideal platform for the morphing demonstration as they require quite small power, whereas the benefit is quite large, besides, the ability to use flexible structures, yet strong enough to support the wing loading[2-4]. These flexible structures could allow different control concepts, hence provide efficient control surfaces that would improve the MAV's agility and maintain smooth flight. However, for a morphing wing to generate its new shape, it would generate aeroelastic forces. These forces would change the shape of the wing, hence influencing the aerodynamic forces. A lot of work has been developed in the last few years concerning the experimental and numerical analysis of flexible MAV wings. In order to study the flight dynamics and structural behaviour of MAV membrane wings, wind tunnel measurements have been used to identify the parameters associated with the flight mechanics[4,5] and the deformations during flight[6,7]. Numerically, full three dimensional computational simulations of the fluid dynamics revealed the effect of unsteady aerodynamics over a membrane MAV wing, hence demonstrating the relation between membrane dynamics and flight performance[8,9].

In this paper, only the aerodynamic design of a MAV wing and its experimental and numerical validations are presented. The non-linear trends due to low Reynolds number and aeroelastic issues are not part of the investigation. The design process considers the combined optimisation of aerodynamic lift and drag using the Multhopp's method based on Prandtl's lifting line theory. The aerodynamic design of such a wing is performed on two steps. Firstly, is the determination of the wing aerofoil spline characteristics and secondly is the determination of the planform of the wing. This wing geometry should satisfy the performance criteria required by the air vehicle and attain the best stall characteristics. The above follows the first problem of the 'Three Basic Problems of Wing Theory' formulated for one separate wing by Prandtl. It is called the design problem in which the lift distribution of the wing is given and wanted is the wing shape (plan form and washout) and its induced drag[10].

The design process is applied to the 'BARQ' MAV for reconnaissance in near field areas. It

https://doi.org/10.1017/S000192400000717X Published online by Cambridge University Press



Figure 1. Initial MAV configuration.

is a conventional wing-tail arrangement MAV with a maximum dimension not exceeding 40cm. It could carry a micro CCD colour zoom camera. The MAV system could be hand held in one brief case including MAV and the mission control system. The 'BARQ' MAV has its first successful flight in July 2009. It has the following performance characteristics:

Endurance:	up to 30min
Flight altitude:	about 50m
Cruise speed range:	up to 70km/hr
Control:	manual flight mode through a ground operator
Launch status:	hand launch

The MAV is initially designed with elliptic wing as shown in Fig. 1. The elliptic wing configuration has the advantage of minimum induced drag values, however the wing uniform lift distribution causes the entire span of the wing to stall simultaneously which is a very dangerous drawback. To compensate, there is a necessity to add some twist distribution to the elliptic wing planform to improve the stall characteristics. However, this would increase the induced drag, reduce the wing efficiency and increase the manufacturing complexity. On the other hand, tapered wings are much easier in manufacturing. Additionally, trapeze wings with certain taper ratios, could almost have the same efficiency as elliptic wings. Hence, it is decided to retain the

https://doi.org/10.1017/S000192400000717X Published online by Cambridge University Press

fuselage, horizontal and vertical tail configurations of the initial MAV and to redesign the wing to have a tapered configuration instead. This new wing geometry should enhance the MAV performance and attain the best stall characteristics. Therefore, the proposed optimisation procedure is applied for the design of the new wing. The lift and drag characteristics of the new wing design as well as the MAV candidate are then validated using wind tunnel measurements. Finally, results are compared with solutions of the Navier-Stokes equations using ANSYS-CFX[11]. These solutions use different turbulence models as the k-ε model, the shear stress transport (SST) model as well as the Reynolds stress model.

2.0 ANALYTICAL PROCEDURE

The main purpose is to design a new wing for the MAV. Hence, a design procedure is presented to optimise the symmetric load distribution satisfying the MAV mission. The objective of the aerodynamic optimisation of wing is to enhance the performance characteristics of the air vehicle during steady level flight. This is accomplished through quantifying the optimum wing geometric parameters including planform and aerofoil spline characteristics.

2.1 Aerodynamic shape optimisation of wing

Since the main purpose of the desired MAV system is reconnaissance, therefore enhancing the air vehicle's range and/or endurance[12-14] allows it to fulfil its mission requirements. The main aerodynamic parameters responsible for enhancing the air vehicle's performance are obtained upon driving the range and endurance equations for electrically-driven air vehicles. According to electrical circuit's laws, the electric current is related to the amount of charge by:

$$I\mathrm{d}t = -\mathrm{d}Q$$

$$\frac{P}{V}\mathrm{d}t = -\mathrm{d}Q \qquad \ldots (1)$$

Hence,

$$\int_0^E \mathrm{d}t = \int_{Q_i}^{Q_f} -\frac{V}{P}\mathrm{d}Q \qquad \ldots (2)$$

To obtain an analogous expression for range, Equation (2) is multiplied by free stream velocity, U.

$$\int_0^R \mathrm{d}s = \int_{Q_i}^{Q_f} -\frac{VU}{P}\mathrm{d}Q \qquad \ldots (3)$$

Since, for level unaccelerated flight the required power is equal to the drag times the velocity and to maintain steady conditions the power available is equal to the required power, taking into consideration that the power mentioned in the above relations is the brake power output which is equal to:

$$P = \frac{P_A}{\eta} \qquad \ldots (4)$$

https://doi.org/10.1017/S000192400000717X Published online by Cambridge University Press

Hence; for level flight where the lift force is equal to the weight force and using Equation (2) the endurance is equal to:

$$E = \int_{Q_i}^{Q_f} -\frac{\eta V}{UD}\frac{L}{W}\mathrm{d}Q \qquad \ldots (5)$$

For preliminary performance analysis, the above equation is simplified for parameter values independent of charge value leading to:

$$E = \frac{\eta V}{UW}\frac{C_L}{C_D}(Q_i - Q_f) \qquad \ldots (6)$$

Therefore, for steady level flight

$$U = \sqrt{\frac{2W}{\rho S C_L}}$$
$$E = \frac{\eta V}{W^{3/2}}\sqrt{\frac{\rho S}{2}}\frac{C_L^{3/2}}{C_D}(Q_i - Q_f) \qquad \ldots (7)$$

A similar derivation will lead to a range equation for the electrically-driven air vehicles as follows:

$$R = \frac{\eta V}{W}\frac{C_L}{C_D}(Q_i - Q_f) \qquad \ldots (8)$$

Thus the aerodynamic quantities that should be optimised are:

- $\left(\frac{C_L}{C_D}\right)_{MAV}$ For range case.
- $\left(\frac{C_L^{3/2}}{C_D}\right)_{MAV}$ For endurance case.

The main contributors to the aerodynamic parameters within the optimisation process are the wing lift and induced drag, which are functions of the lift distribution on the wing, which depends on the particular wing being considered. The prediction of the zero-lift and induced drags for the different air vehicle's components, except the wing induced drag, are modeled by Class II methods based on USAF Stability and Control Datcom which applies to airplanes with essentially straight, tapered wings[15,16]. However, the wing's aerodynamic characteristics are obtained using Multhopp's method based on Prandtl's lifting line theory.

2.2 Spanwise load distribution using Multhopp's method based on lifting line theory.

The classical lifting line theory developed by Ludwig Prandtl and published in 1918 is the first analytical method to satisfactorily predict the performance of a lifting wing[17,18]. Moreover, until the development of the digital computer in the early 1960s, it was the only analytical tool

https://doi.org/10.1017/S000192400000717X Published online by Cambridge University Press

available for wing design. Early comparisons between results predicted from the lifting line theory and experimental data showed excellent agreement for wings with aspect ratio greater than 4. Even with modern computational fluid dynamics (CFD) it is difficult to improve on the induced drag predictions derived from the lifting line theory. Prandtl lifting line theory is still widely used today, because it has the advantage of yielding closed form solutions. Such solutions are not only many order of magnitude faster to evaluate than modern CFD solutions, but they provide greater insight into how wing design parameters affect wing performance.

The equation for the determination of the spanwise load distribution of a given wing of finite span, introduced by Prandtl[19-26], compares the reduced lift at a cross section y of a finite span wing with the lift at the same cross section of an infinitely long wing. This reduced lift is due to the change of the incident flow direction that results from the downwash velocity induced by the free vortices, hence, a profile cross section of a wing of finite span behaves like that of a wing of infinite span (plane flow) at an angle of incidence α_e. The geometric angle-of-attack $\alpha(y)$, measured from the zero-lift position, the effective angle $\alpha_e(y)$, and the induced angle $\alpha_i(y)$ are related by[19-26]:

$$\alpha(y) = \alpha_e(y) + \alpha_i(y) \quad \ldots (9)$$

The effective angle-of-attack, $\alpha_e(y)$, is obtained with the help of the Kutta-Joukowsky theorem, while the induced angle-of-attack, $\alpha_i(y)$, is obtained from $\alpha_i(y) = w_i(y)/U$, where, w_i is the distribution of the induced downwash velocity along the span obtained by applying the Biot-Savart law to the semi infinitely long free vortex behind the wing and integrating over the area of the free vortices[19-26].

$$\alpha_e = \frac{2\Gamma(y)}{Uc(y)a_{o,w}} \quad \ldots (10)$$

$$\alpha_i(y) = \frac{1}{4\pi U}\int_{-b_w/2}^{b_w/2} \frac{d\Gamma}{dy'}\frac{dy'}{y-y'} \quad \ldots (11)$$

Introducing Equations (10) and (11) into Equation (9) yields the determination of the circulation distribution which is a linear integral equation for the circulation distribution $\Gamma(y)$.

Solution to the problem of determining the spanwise lift distribution for wings has been presented by Multhopp[19,20]. Multhopp's approach was to find the local circulation at several preselected points instead of a completely general solution. A simple method to determine a satisfactory spanwise distribution of arbitrary points where more points near the tips, where the curve changes most rapidly are required, is given according to the relation[19,20]:

$$\theta_\nu = \nu\frac{\pi}{m+1} \quad \ldots (12)$$

The span station is then[19,20]:

$$\zeta_\nu = \frac{b}{2}\mathrm{Cos}(\theta_\nu), \quad \overline{\zeta}_\nu = \mathrm{Cos}(\theta_\nu) \quad \ldots (13)$$

https://doi.org/10.1017/S000192400000717X Published online by Cambridge University Press

The local effective angle-of-attack at station ν is equal to the local geometric angle-of-attack plus the effect of all the shed vortices[19,20]:

$$\alpha_{ev} = b_v \gamma_v = \alpha_v + \sum_{1}^{m} b_{vn} \gamma_n \quad \ldots (14)$$

where b_{vn} is a Multhopp coefficient accounting for the increment of induced angle at station v due to vortex at station n, while b_v is a Multhopp coefficient that accounts for the effect of the circulation at station ν on that at station n and is equal to $[2\,\lambda_v / a_o\,(\nu)] + b_{vv}$. In Multhopp's actual solution to obtain the values for the coefficients it develops that[19,20]:

$$b_{vv} = \frac{m+1}{4\,\mathrm{Sin}(\theta_v)} \quad \ldots (15)$$

$$b_{vn} = \frac{\mathrm{Sin}(\theta_n)}{(\mathrm{Cos}(\theta_v) - \mathrm{Cos}(\theta_n))^2} \frac{1-(-1)^{v-n}}{2(m+1)} \quad \ldots (16)$$

Equation (14) can now be solved for local non-dimensional circulation γ, hence, the local lift coefficient becomes known through[19,20]:

$$c_{l,w} = 2\lambda_w \gamma \quad \ldots (17)$$

And the equation for the total wing lift coefficient is[19,20]:

$$C_{L,w} = AR_w \int_{-1}^{1} \gamma(\bar{\zeta}) \mathrm{d}\bar{\zeta} \quad \ldots (18)$$

The induced drag coefficient is[19,20]:

$$C_{Di,w} = AR_w \int_{-1}^{1} \gamma(\bar{\zeta}) \alpha_i \mathrm{d}\bar{\zeta} \quad \ldots (19)$$

Although being a very weak source of lift compared to the wing, the other secondary source of lift accounted for is that produced by the horizontal tail. Its lift is added to that produced by the wing to obtain the total MAV lift during the optimisation process. It could be evaluated from[15,16]:

$$C_{L,ht} = a_{o,ht} \frac{S_{ht}}{S_w} (\alpha(1-(\frac{\partial \varepsilon}{\partial \alpha})) - \varepsilon_o + i_{ht}) \quad \ldots (20a)$$

$$\alpha = \alpha_w - i_w \quad \ldots (20b)$$

2.3 Application of the optimisation process to the MAV's wing

Beside the low subsonic flight regime, the miniature dimensions of the MAV yield to the choice of low Reynolds number aerofoils to be used during the optimisation process. The wing's profile (aerofoil) is allowed to be chosen from the set of low Reynolds number aerofoils elaborated by Richard Eppler (E64, E66, E211 and E212)[27]. Also, a straight planform wing configuration is

https://doi.org/10.1017/S000192400000717X Published online by Cambridge University Press

chosen; hence only three design variables could serve in completely describing the wing planform shape. These three variables are chosen to be the wing span, aspect ratio and taper ratio. During the optimisation process, The wing span has an upper bound value of 40 (cm) to avoid violation with the mission specifications of the MAV, while the wing aspect ratio has a lower bound of 4 to be in accordance with the assumptions of the lifting line theory. The wing taper ratio is allowed to change between the values 0·4 till a unity value.

The optimisation problem is formulated so as to enhance the performance of the MAV. The optimisation process is implemented twice; one for maximising the range performance through maximising the ratio (C_L/C_D) and the other for maximising the endurance performance through maximising the ratio ($C_L^{3/2}/C_D$). The values of the design variables, describing the geometric wing planform and aerofoil characteristics are obtained for both optimisation processes under the constraint of avoiding wing stall; to have a design point away enough from the stall limits and to control the spanwise location of the start of the stall. Ensuring a smooth and safe flight is also an important consideration for MAVs flight. Hence, the wing's maximum lift is constrained to be at least greater than the maximum lift the MAV requires by 10%. These conditions are very important in deriving the objectives towards the obtained optimal values, hence, determining the optimal symmetric load distribution satisfying the MAV requirements. The stall angle-of-attack is obtained analytically by comparing the spanwise distribution of cc_l with the spanwise distribution of $cc_{l,max}$ [20]. The $cc_{l,max}$ distribution will not be constant owing to the changing of both the chord and the Reynolds number. The procedure embraces plotting the cc_l and $cc_{l,max}$ distributions on one sheet and increasing $C_{L,w}$ progressively until the curve cc_l touches that of $cc_{l,max}$. The spanwise location of the tangency is then the spanwise location of the start of the stall and the angle-of-attack corresponding to $C_{L,w}$ is the stall angle-of-attack.

Based on the 'Modified Feasible Directions Gradient Based Algorithm', the optimisation process is implemented in the general purpose optimisation system, VisualDOC[28-30]. The modified method of feasible directions is a nonlinear optimisation algorithm that combines the features of the method of feasible directions and the generalised reduced gradient method. The algorithm uses the direction-finding subproblem from the method of feasible directions to find a search direction that is equivalent to that of the generalised reduced gradient method but without the need of the large number of slack variables associated with inequality constraints. The modified method of feasible directions used in VisualDOC incorporates the best features of both methods, it is designed specifically for inequality constrained problems, it does not increase the dimensionality of the design problem by adding slack variables to the inequality constraints and it requires only the gradients of the active constraints set, thus reducing both computational effort and computer storage. The method repeats the sub-problem of finding a new usable-feasible search direction, followed by continued search until no search direction can be found that will improve the design without violating one or more constraints.

The aerodynamic problem illustrated previously is solved in which the configuration of the MAV components (fuselage, horizontal and vertical tail) is fixed and their values during the optimisation process are taken as that of the initially designed MAV. The wing configuration is allowed to change according to the optimisation problem mentioned till reaching the optimum wing configuration. The convergence of the optimisation process is shown through the time histories of the objective functions in Figs 2 and 3.

The obtained results for both range and endurance optimised configurations are very close from each other from the point of view of dimensions and maximum objective values. Therefore, a final configuration is taken by rounding off the basic dimensions obtained from both optimisation processes to simplify the manufacture procedure through having simple and clean

https://doi.org/10.1017/S000192400000717X Published online by Cambridge University Press

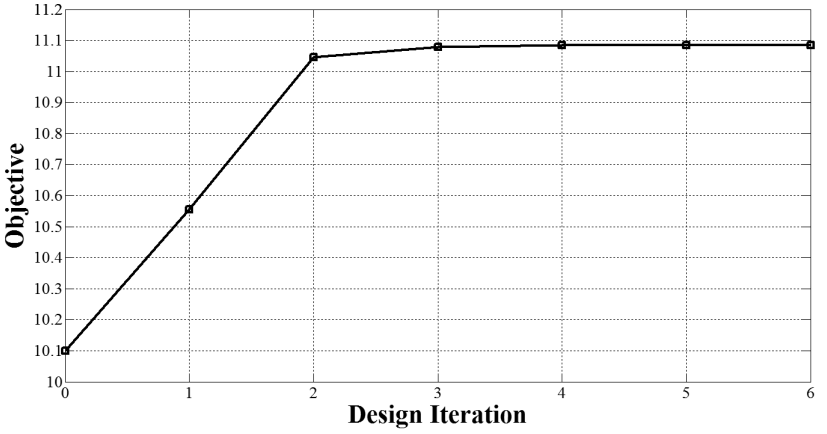


Figure 2. Objective function history during range optimisation.

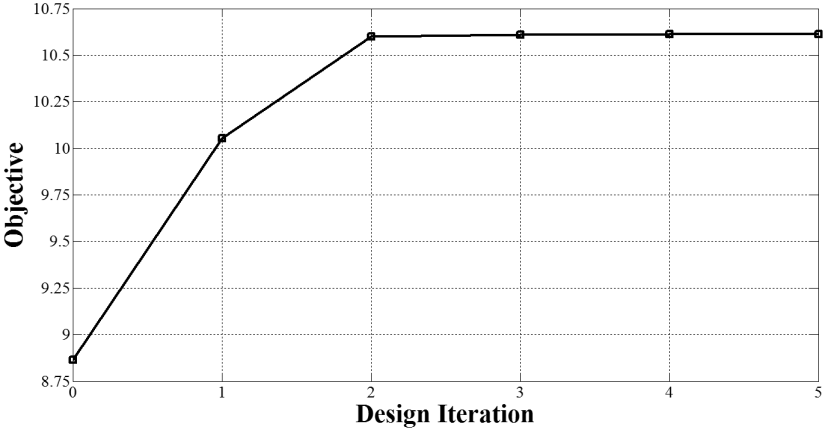


Figure 3. Objective function history during endurance optimisation.

dimensions and without losing a lot in the performance objectives. The final wing configuration is also allowed to have a small sweep angle for the geometric improvement of the wing planform shape. The values of the wing design variables, geometric dimensions, constraints and the aerodynamic objectives of both range and endurance optimised configurations as well as the final configuration are presented in Table 1 and a CAD model for the final wing mounted on the MAV is presented in Fig. 4. The final wing configuration has a lift coefficient of 0·75 and an induced drag value of 0·0363 at the condition of maximum (C_L/C_D). It also has a lift coefficient of 1·0084 and an induced drag value of 0·0657 at the condition of maximum ($C_L^{3/2}/C_D$). Both conditions are at an adequate margin from the stall limit.

3.0 EXPERIMENTAL SETUP

Using the MAV CAD model shown in Fig. 4, a wind tunnel one to one model is manufactured using CNC machine. This measurement model is made from aluminium and is shown in Fig.

https://doi.org/10.1017/S000192400000717X Published online by Cambridge University Press

Table 1
Optimal values of the design variables, geometric dimensions, constraints and objective functions

Parameter	Range optimised configuration	Endurance optimised configuration	Final configuration
Aerofoil	E212	E212	E212
Wing span, b_w (cm)	40	39.9	40
Wing aspect ratio, AR_w	5·054	5·065	5
Wing taper ratio, TR_w	0·6522	0·6275	0·6
Wing area, S_w (cm^2)	317	316	320
Wing root chord, $c_{r,w}$ (cm)	9·582	9·705	10
Wing tip chord, $c_{r,w}$ (cm)	6·249	6·089	6
Wing quarter chord sweep angle (deg.)	-	-	3
$C_{L,w,max}/C_{L,MAV,max}$	1·1002	1·0997	1·1118
$(C_L^{3/2}/C_D)_{MAV}$	10·6271	10·6361	10·53
$(C_L/C_{D)MAV}$	11·09	11·08	11·02++

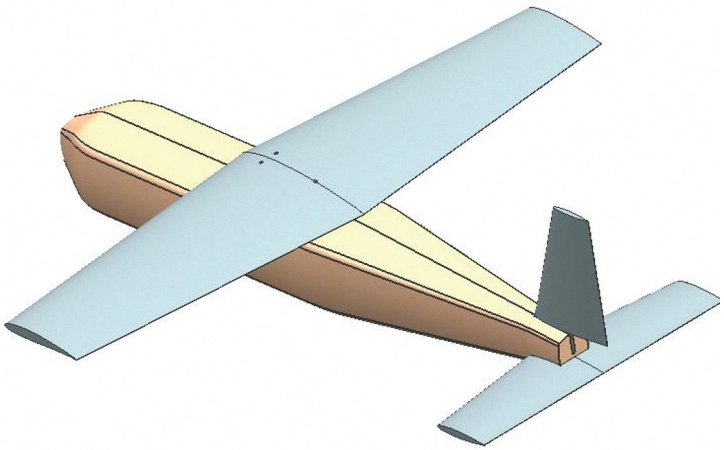


Figure 4. CAD model for the final wing configuration installed on MAV.

5. It is a totally rigid model for the aerodynamic concept validation without encountering the aeroelastic or flexibility issues. Wind tunnel measurements are conducted at the low speed wind tunnel in the Aerospace Engineering Department, Cairo University. It is an open circuit tunnel with maximum flow speed of 50m/sec and has a test section of dimensions 0·8 ×1·2 × 2·5m equipped with a three component balance. The measurements are conducted at a speed of 42 m/sec to amplify the generated forces so the balance could sense them accurately especially at flow conditions where the generated forces become of low magnitudes. Figure 6 shows the wind tunnel test section with the model mounted in.

In order to assure good experimental data, our first temptation may be to call the data 'good' if they agree well with the theory. But, theory is simply a model intended to mimic the behaviour of the real situation. In order to ensure the measurement results, measurements are

https://doi.org/10.1017/S000192400000717X Published online by Cambridge University Press



Figure 5. Wind tunnel measurements MAV model.

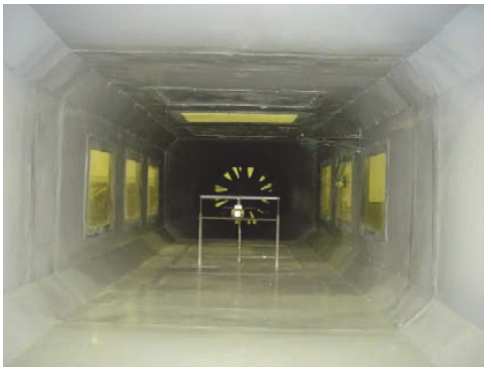


Figure 6. Model mounted in the wind tunnel test section.

repeated as much as possible to assure its repeatability and be able to estimate their uncertainty using statistical tools. It is of importance to mention that errors could not be evaluated as a true value of the measured quantity is not well known; hence, uncertainty checks should be accomplished[31,32]. During the experiment, care is taken to avoid bias errors such as human and loading errors or any kind of illegitimate errors due to mistakes. Precision errors that could be caused by factors such as disturbances to the equipment or fluctuating experimental conditions are accounted for through evaluating precision uncertainty using the confidence intervals for small samples. Hence, the wing and MAV measurements are carried out four times in both an increasing and a decreasing angle-of-attack sense to have a total of eight measurements for each angle-of-attack. Each angle-of-attack measurement has a 720 readings sample. The mean value of this sample is then used to calculate the uncertainty of the eight measurements using:

$$P_x = t_{\alpha/2,N-1}\frac{S_x}{\sqrt{N}} \qquad \ldots (21)$$

The uncertainty checks of the eight experimental runs are first presented. This is followed by comparison to the previously obtained theoretical results. It is of importance to mention that the walls, weight and adaptor effects are always considered and all of the obtained experimental results are corrected from their effects.

3.1 Wing results

Figure 7 presents the obtained precision uncertainty values that are at a 95% confidence level. It is observed that the drag uncertainty values are better and are almost constant; with a mean uncertainty value of 1·1%, while, the lift uncertainty has a mean value of 12·37%. It is also observed that the uncertainty and the standard deviation values increase as the angle-of-attack increases which is predicted.

Figure 8 shows a comparison between the obtained analytical wing lift from the lifting line theory and the wind tunnel measurements. It is observed that there is a very good agreement in the lift curve slope, zero lift angle-of-attack which adds to the potential merits of the lifting line theory. Experimental results also showed the stall variations which are difficult to predict analytically except for the stall angle of angle-of-attack which is exactly as the analytical calculation. The stall angle-of-attack is 11 degrees measured from the wing chord line. It is also observed that the maximum lift is lower than that predicted analytically.

https://doi.org/10.1017/S000192400000717X Published online by Cambridge University Press

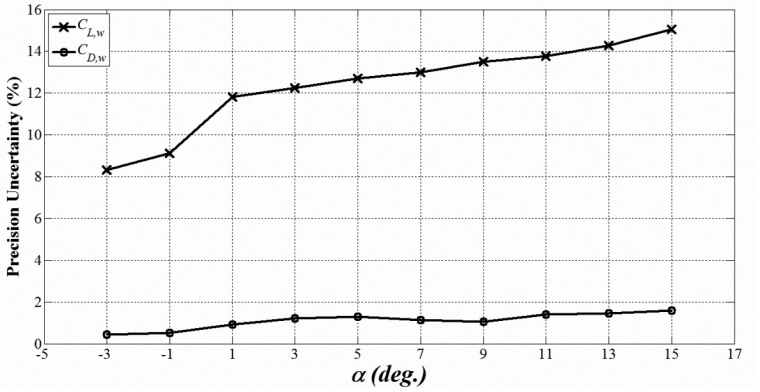


Figure 7. Experimental measurements precision for wing.

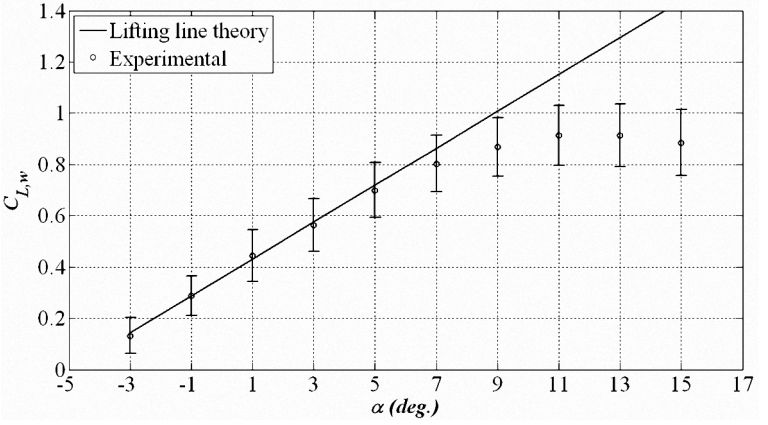


Figure 8. Comparison between analytical and experimental lift results for wing.

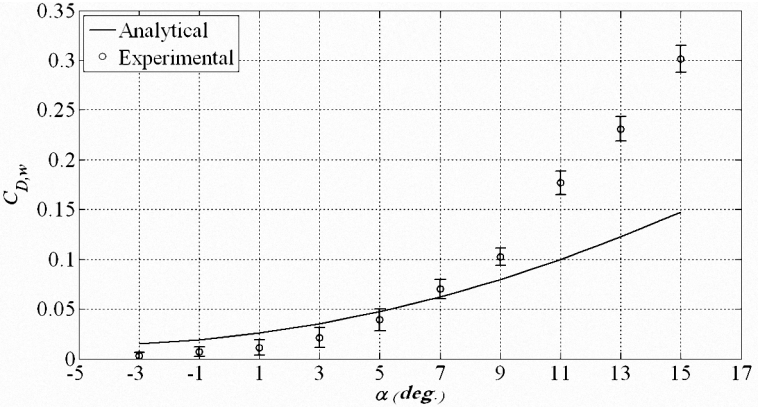


Figure 9. Comparison between analytical and experimental drag results for wing.

https://doi.org/10.1017/S000192400000717X Published online by Cambridge University Press

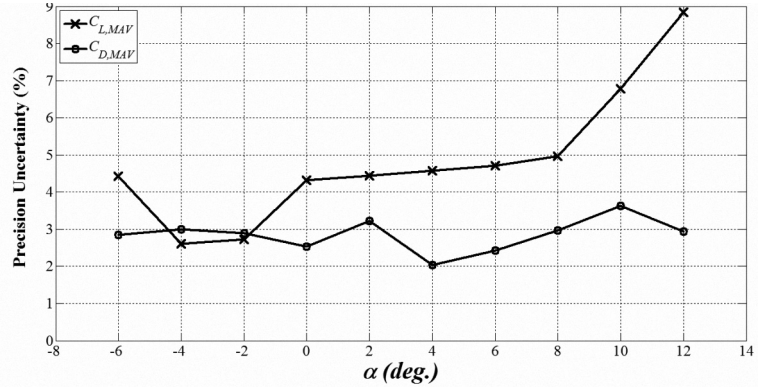


Figure 10. Experimental measurements precision for MAV.

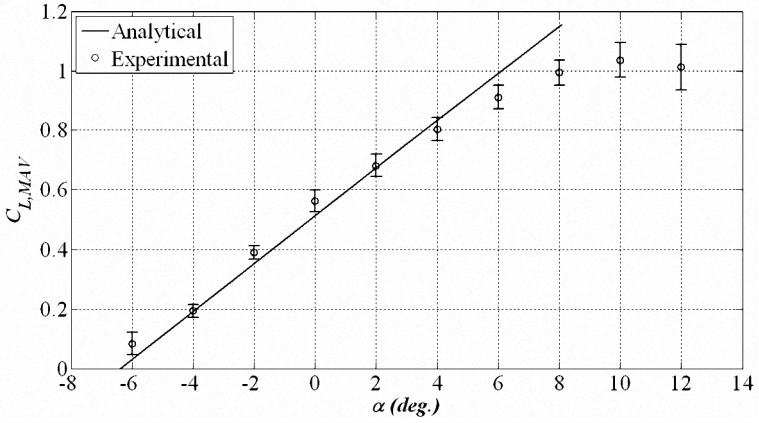


Figure 11. Comparison between analytical and experimental lift results for MAV.

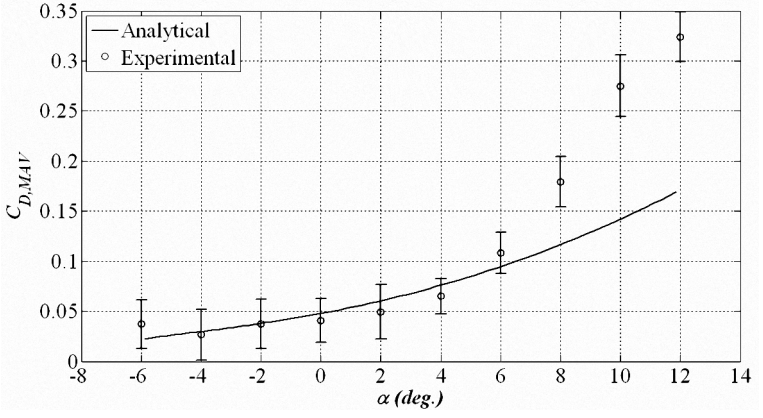


Figure 12. Comparison between analytical and experimental drag results for MAV.

Figure 9 shows a comparison between the obtained analytical drag and the experimental results in which an acceptable matching is observed between them. The analytical procedures (zero-lift drag modelled by Class II methods based on USAF Stability and Control Datcom and induced drag

https://doi.org/10.1017/S000192400000717X Published online by Cambridge University Press

modelled by lifting line theory) seem to overestimate the drag values at small angle-of-attacks, which is quite safe. However, experimental results deviate from the analytical ones considerably after the stall angle-of-attack.

It is believed that some of the deviation between the analytical and experimental results in the wing case is due to the effect of balance struts and adaptor on the wing characteristics as they have considerable size with respect to the wing.

3.2 MAV results

Figure 10 presents the experimental drag measurements uncertainty values which are almost constant with a mean uncertainty value of 2·8%, while, lift uncertainty has a mean of 4·8%. It is observed that the uncertainty values for the MAV lift are better than that of the wing proving what we claimed that the small size of the wing would affect its measurements. While, the MAV drag uncertainty values are higher than that of the wing due to the effects of various MAV components. This is also clear through the smaller variance of lift readings and the larger variance of drag readings of the MAV at each angle-of-attack compared to the wing case. However, the obtained uncertainty values are within the acceptable range allowing the experimental results to validate the analytical method used in developing the current MAV.

Figure 11 shows a comparison between the obtained analytical lift (due to the MAV wing and horizontal tail) and the experimental results for the MAV candidate, where, very good agreement in the lift curve slope, zero lift angle-of-attack as well as the maximum lift value is observed between the analytical and the experimental results. The experimental results predicted the stall angle-of-attack at a slightly higher angle-of-attack from the analytical calculation (The MAV stall angle-of-attack is 8 degrees based on Equation (20-b)) which is quite safe.

Figure 12 shows a comparison between the obtained analytical drag (zero-lift and induced drags for the different air vehicle's components, except the wing induced drag, are modelled by Class II methods based on USAF Stability and Control Datcom, while the wing induced drag is modelled by the lifting line theory) and the experimental results for the MAV candidate in which a very good matching is observed between them. Once more, experimental results deviate from the analytical ones considerably after stall.

4.0 CFD APPROACH

In this section, the analytical solutions and the experimental results are compared with solutions to the Navier-Stokes equations solved with finite elements using ANSYS-CFX. Ultimately, though, it approaches form 'control volume' equations that ensure exact conservation of flow quantities, a vital property for accurate CFD simulations. In what follows; CFD solutions are presented using in which a steady formulation is employed. All results are obtained at the design free stream velocity of 15·83m/sec.

4.1 Wing simulations

4.1.1 Grid resolution and boundary conditions

Mesh sequencing is employed in the solution procedure of the wing using coarse, medium, normal and fine grids having the properties given in Table 2. The nodes are distributed over a computational domain of a cube shape that extends 15 chord lengths. Inflow/outflow boundary

https://doi.org/10.1017/S000192400000717X Published online by Cambridge University Press

Table 2
Grid sizes for wing CFD analysis

	Coarse	Medium	Normal	Fine
Nodes	45,862	96,858	212,586	632,620
Elements	262,947	551,368	1,210,772	3, 699,259

conditions are specified as well as wall boundary condition over the wing body. Figures 13 and 14 shows the course and the fine grid shape over the wing.

Before any discretisation error estimation is calculated, it is ensured that iterative convergence is achieved and the lift and drag coefficients has reached a stable constant value with six order of magnitude decrease in the normalised residuals for each equation solved. Using converged results from the different grids the dependence of the solution on the mesh size, the procedure described in Refs 33 and 34 to evaluate the numerical accuracy of the results is applied. For the sake of completeness this procedure is briefed in the following:

Step 1: Define a representative cell, mesh or grid size h. For three dimensional calculations:

$$h = \left[\frac{1}{N}\sum_{i=1}^{N}\Delta V_i\right]^{1/3} \quad \ldots (22)$$

Where; ΔV_i is the volume of the ith cell, and N is the total number of cells used for the computations.

Step 2: Select three significantly different set of grids, and run simulations to determine the values of key variables important to the objective of the simulation study, for example, a variable φ critical to the conclusions being reported. It is desirable that the grid refinement factor, $r = h_{coarse}/h_{fine}$, be greater than 1·3. This value of 1·3 is based on experience, and not on formal derivation.

Step 3: Let $h_1 < h_2 < h_3$ and $r_{21} = h_2/h_1$, $r_{32} = h_3/h_2$, and calculate the apparent order, p, of the method using the expression:

$$p = \frac{1}{\ln(r_{21})}\left|\ln\left|\varepsilon_{32}/\varepsilon_{21}\right| + q(p)\right| \quad \ldots (23a)$$

$$q(p) = \ln\left(\frac{r_{21}^{p} - s}{r_{32}^{p} - s}\right) \quad \ldots (23b)$$

$$s = sign(\varepsilon_{32}/\varepsilon_{21}) \quad \ldots (23c)$$

Where; $\varepsilon_{32} = \varphi_3 - \varphi_2$, $\varepsilon_{21} = \varphi_2 - \varphi_1$, φ_k denoting the solution on the kth grid. Equation (23) is solved using fixed-point iteration, with the initial guess equal to the first term.

Step 4: Calculate and report the following error estimates:

https://doi.org/10.1017/S000192400000717X Published online by Cambridge University Press

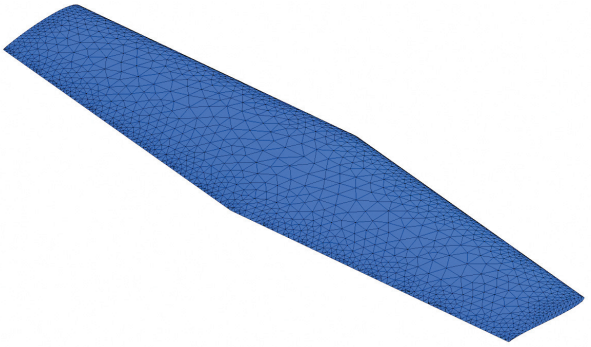


Figure 13. Wing coarse grid.

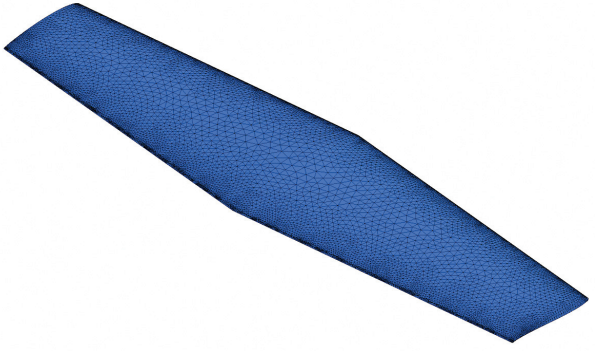


Figure 14. Wing fine grid.

1- Approximate relative error:

$$e_a^{21} = \left| \frac{\varphi_1 - \varphi_2}{\varphi_1} \right| \quad \ldots (24)$$

2- Fine grid convergence index:

$$GCI_{fine}^{21} = \frac{1 \cdot 25 e_a^{21}}{r_{21}^p - 1} \quad \ldots (25)$$

The previous accuracy checking procedure is adapted to the coarse, medium and normal grids as well as the medium, normal and fine grids with the last having a r_{21} value of 1·45 and a r_{32} value of 1·3. This shows very satisfactory grid convergence history, where the lift and drag relative error values at different angles-of-attack as well as the fine grid convergence index (GCI) are shown in Table 3. The GCI method is an acceptable and recommended method that has been evaluated over several hundred CFD cases[33,34]. It is clear that the GCI values attains high values in high negative angles-of-attack. They also attain higher values in stall conditions. While, these values drops abruptly in the flying range of angles of attack and are all highly acceptable.

Figures 15 and 16 shows the lift and drag grid convergence results, where, it is concluded that using the normal grid in CFD simulations is optimum for computation efficiency as finer discreti-

https://doi.org/10.1017/S000192400000717X Published online by Cambridge University Press

Table 3
Lift and drag relative error and fine grid convergence index values

α (deg)	$C_{L,w}$ error (%)	$C_{D,w}$ error (%)	$C_{L,w}\ GCI^{21}_{fine}$ (%)	$C_{D,w}\ GCI^{21}_{fine}$ (%)
–5	21	11	3·1	1·35
–3	3·9	8·7	0·57	0·85
–1	1·9	3·8	0·27	0·25
1	1·2	1·3	0·15	0·061
3	0·8	1	0·08	0·058
5	0·5	1·3	0·04	0·15
7	0·4	1·9	0·02	0·35
9	0·2	2·5	0·002	0·71
11	0·15	3·2	0·0016	1·3
13	0·7	4·2	0·068	2·7

sation does not improve the solution significantly. In addition to the grid convergence analysis discussed above, which is performed on a fixed computational domain extending 15 chord lengths, different computational domain sizes where analysed of 5 and 10 chord lengths and the solution appears to converge at 15 chord lengths. Results obtained for larger computational domain of 20 chord lengths revealed almost no change when compared to the results obtained from the 15 chord domain. Consequently, the 15 chord domain is deemed sufficient for the remainder of the computation.

4.1.2 Turbulence models

In order to check the problem attitude upon using different turbulence models and to remove any sources of numerical instability, a study of the solution under different turbulence models is adopted using the normal grid. These models include the Reynolds Stress model and the simpler two-equation turbulence models as the k-ε and the shear stress transport (SST) model of Menter[35] which works by solving a turbulence/frequency-based model, k–ω at the wall and k-ε in the bulk flow. A blending function ensures a smooth transition between the two models. In a NASA Technical Memorandum[36], SST is rated the most accurate model for aerodynamic applications due to its improved eddy viscosity formulation, its automatic wall function, being more proper model for separated flows and being less sensitive to y^+. Also, from a computational point of view it is more efficient than the Reynolds Stress model as it has fewer variables to solve. As for the near wall treatment, a scalable wall function formulation which can be applied on arbitrarily fine meshes is used[11]. While, as mentioned, for the SST model an automatic near wall treatment is used, which allows for a smooth shift from a low Reynolds number form to a wall function formulation[11]. The values of y^+ on the wall is checked to be in the recommended range for each model, hence ensuring proper near wall resolution[11].

Figures 17 and 18 show that the obtained CFD solutions are to a great extent similar to the previously obtained analytical results especially for the lift characteristics, where, there is almost no significant difference between turbulence models. The difference between turbulence models appears in the drag characteristics; however, they share the same trend. This is predicted as the lift characteristics depend on mainly mathematical procedures, while, the drag characteristics depend on the physical model used. The k-ε model showed to give the worst matching with the

https://doi.org/10.1017/S000192400000717X Published online by Cambridge University Press

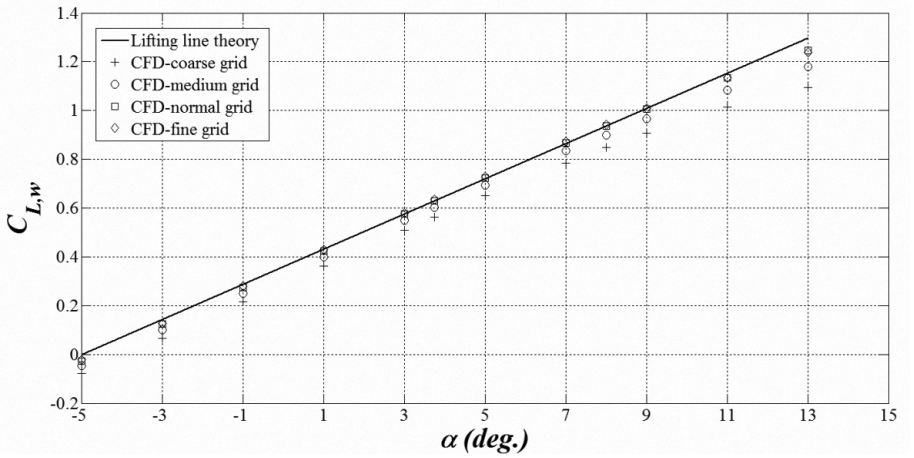


Figure 15. Wing lift CFD results, grid convergence.

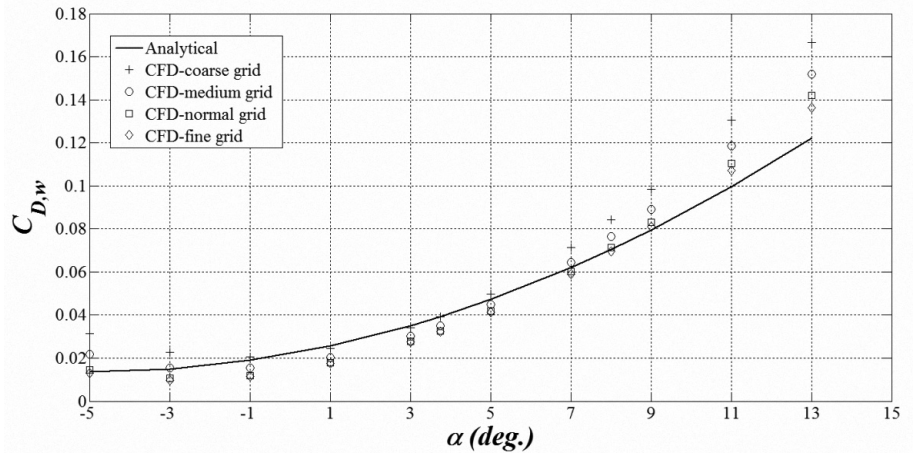


Figure 16. Wing drag CFD results, grid convergence.

analytical results, while, the SST model is the best matching model with the analytical results. The Reynolds stress model is the best matching model with the experimental results along most of the flying angles of attack; however, the experimental results deviate significantly from all turbulence models predictions beyond stall.

4.2 MAV simulations

Similar grid convergence studies are adopted for CFD simulations of the MAV candidate reaching to a normal grid that has 1,070,200 nodes and 6,231,862 elements. Different turbulence models are also used for the MAV CFD simulation. Figures 19 and 20 show the pressure distribution on the MAV using the SST model at design angle-of-attack. Figure 21 shows a very good agreement between the analytical, CFD and experimental lift results. The analytical results are stopped at the stall angle-of-attack. The lift curve slopes are almost the same. However, it is observed that; the CFD solutions underestimate the lift values slightly.

https://doi.org/10.1017/S000192400000717X Published online by Cambridge University Press

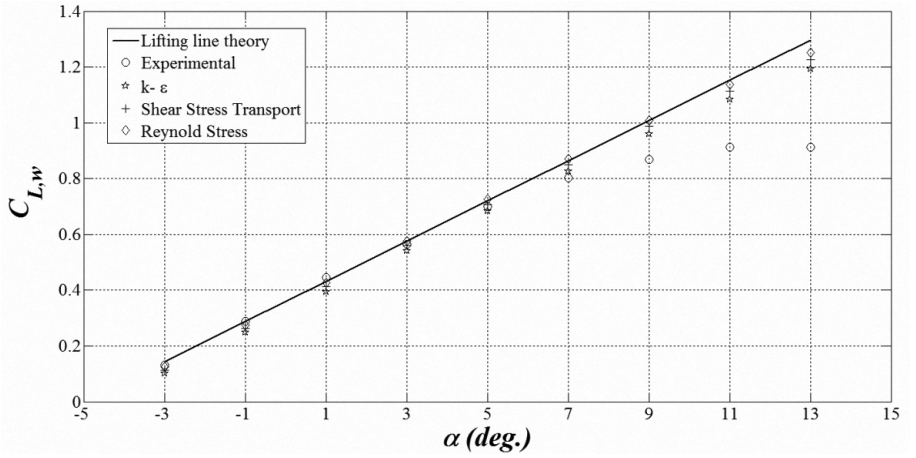


Figure 17. Wing lift CFD results, turbulence models.

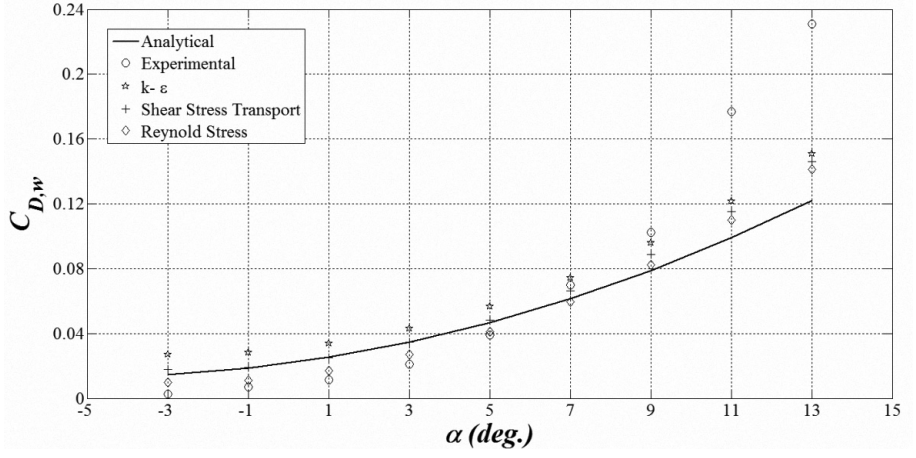


Figure 18. Wing drag CFD results, turbulence models.

Figure 22 shows also a good matching between the analytical, CFD and the experimental drag results for most of the flying angles-of-attack, however, CFD solutions show to overestimate the drag values. Similar to the wing results, the *k*-ε model shows to give the worst matching with the analytical results, the SST model is the best matching model with the analytical results. The Reynolds stress model is the best matching model with the experimental results along most of the flying angles of attack. Also, CFD solutions show to be more matching with the experimental results in the vicinity of the zero lift angle-of-attack, where the drag value is much higher than that predicted analytically. However, it should be noted that the presence of a flight condition in this region is very difficult. Finally, the CFD solutions underestimate the experimental results at angles-of-attack beyond the stall angle-of-attack predicted analytically.

Figure 23 presents a comparison between various evaluation methods for the MAV design objective (lift to drag ratio). The analytical procedure almost matches with the experimental results regarding the flight condition of global maximum objective. However, the experimental

https://doi.org/10.1017/S000192400000717X Published online by Cambridge University Press

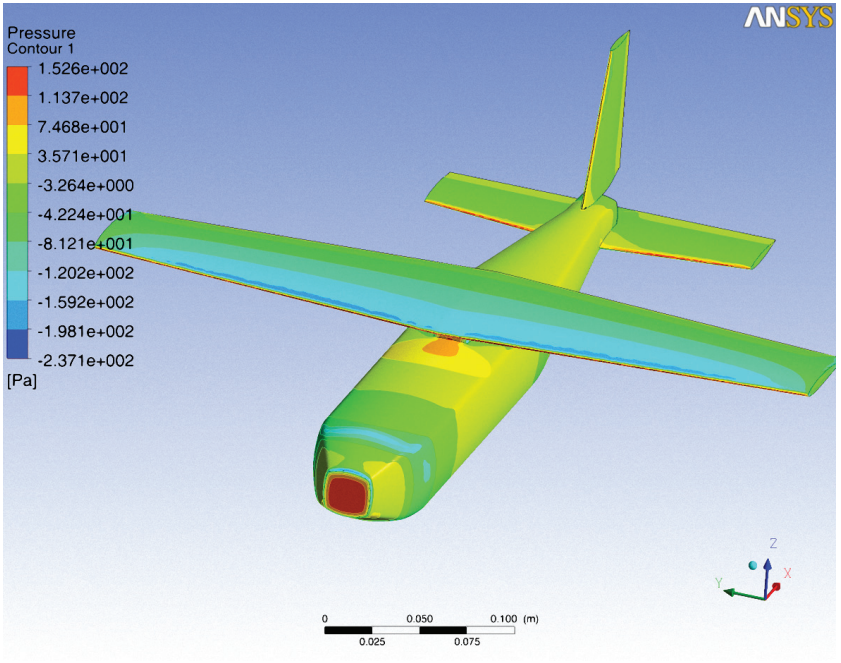


Figure 19. Pressure distribution on the MAV surface at 2·4 deg angle-of-attack, U = 15·83 m/sec, upper surface.

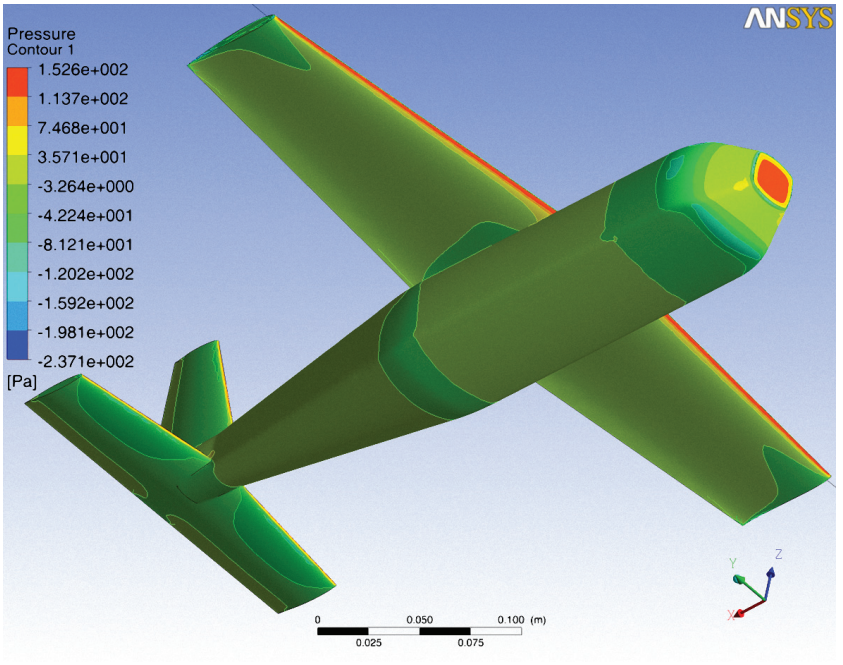


Figure 20. Pressure distribution on the MAV surface at 2·4 deg angle-of-attack, U = 15·83 m/sec, lower surface.

https://doi.org/10.1017/S000192400000717X Published online by Cambridge University Press

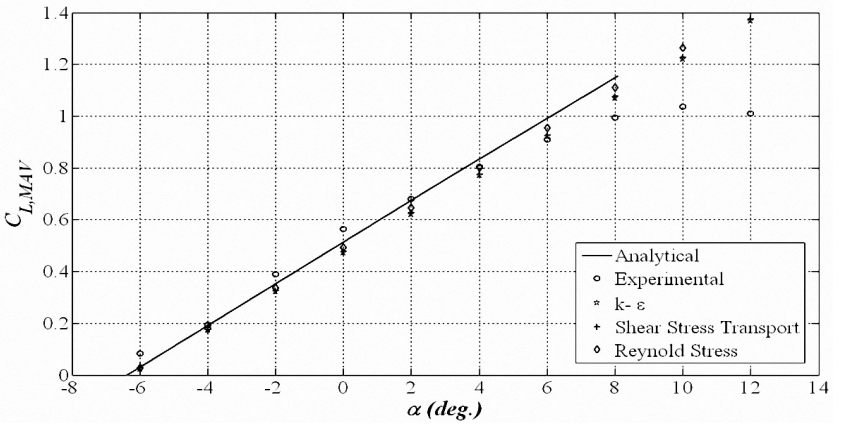


Figure 21. MAV lift results.

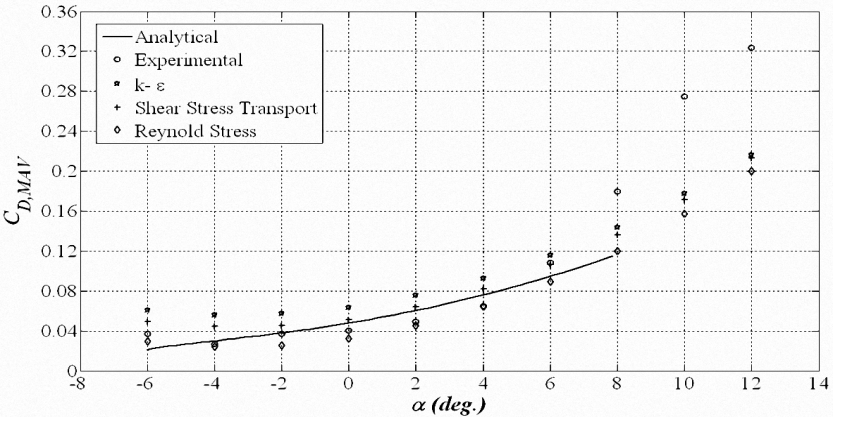


Figure 22. MAV drag results.

results overestimate the maximum objective value, which is quite positive. Once again, the SST model is the best matching model with the analytical results. The Reynolds stress model is the best matching model with the experimental results along most of the flying angles of attack, however; the extremely high computational cost required for the evaluation of the CFD solutions are non-comparable with that required for the analytical procedure.

5.0 CONCLUSIONS

The proposed aerodynamic design optimisation of MAV wing and its experimental and numerical validations show that:

1. The derived range and endurance equations for electrically driven micro air vehicles are valid.
2. The use of Multhopp's procedure based on Prandtl's lifting line theory can be easily used for such type of wing for this category of air vehicles.
3. The modified feasible directions gradient based optimisation algorithm converges rapidly for the solution of wing design of MAV.

https://doi.org/10.1017/S000192400000717X Published online by Cambridge University Press

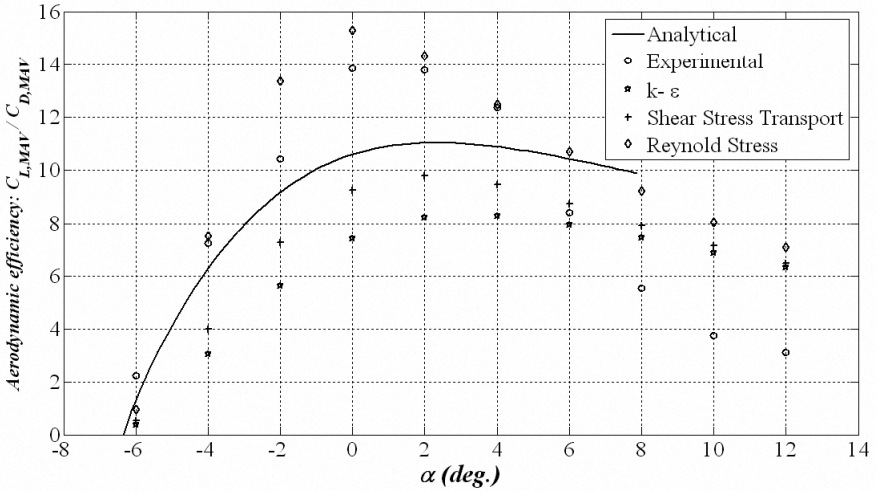


Figure 23. MAV lift to drag ratio results.

4. Experimental results are strongly validating the design technique used in developing the current MAV candidate.
5. CFD solutions adopted give almost perfectly matching results for the lift characteristics and acceptable results for the drag characteristics depending on the used turbulence model. However, they need significantly higher computational cost compared to the developed analytical design procedure.
6. The shear stress transport turbulence model shows to be the most matching model with the developed analytical procedure. While, the Reynolds stress model shows to be the most matching with the obtained experimental results.

ACKNOWLEDGEMENTS

The authors would like to thank Osama S. Mohammady, Islam H.S. ElQatary and Sameh S. Ali from the Aerospace Engineering Department, Cairo University for the many hours of work invested in the setup of the experimental part of this work.

REFRENCES

1. GRASMEYER, J.M. and KEENNON, M.T. Development of the Black Widow micro air vehicle, January 2001, AIAA Paper 2001-0127.
2. IFJU, P.G., JENKINS, D.A., ETTINGER, S., LIAN, Y., SHYY, W., and WASZAK, M.R. Flexible-wing based micro air vehicles, January 2002, AIAA Paper 2002-0705.
3. ABDULRAHIM, M., GARCIA, H. and LIND, R. Flight characteristics of shaping the membrane wing of a micro air vehicle, *AIAA J Aircr*, January–February 2005, **42**, (1), pp 131–137.
4. STANFORD, B., ABDULRAHIM, M., LIND, R. and IFJU, P. Investigation of membrane actuation for roll control of a micro air vehicle, *AIAA J Aircr*, May-June 2007, **44**, (3), pp 741–749.
5. WASZAK, M.R., JENKINS, L.N., and IFJU, P. Stability and control properties of an aeroelastic fixed wing micro air vehicle, 2001, AIAA Paper 2001-4005, AIAA Atmospheric Flight Mechanics Conference, 6-9 August 2001, Montreal, Canada.

https://doi.org/10.1017/S000192400000717X Published online by Cambridge University Press

6. FLEMING, G.A., BARTRAM, S.M.,WASZAK, M.R. and JENKINS, L.N. Projection moire interferometry measurements of micro air vehicle wings, 2001, SPIE Paper 4448-16, Society of Photo-Optical Instrumentation Engineers International Symposium on Optical Science and Technology, 29 July-3 August 2001, San Diego, CA, USA.
7. ALBERTANI, R., HUBNER, P., IFJU, P., LIND, R. and JACKOWSKI, J. Experimental aerodynamics of micro air vehicles, 2004, Paper 2004-01-3090, Society of Automotive Engineers World Aviation Congress and Exhibition, Reno, NV, USA.
8. LIAN, Y., SHYY, W. and IFJU, P. Membrane wing model for micro air vehicles, *AIAA J*, 2003, **41**, (12), pp 2492–2494.
9. LIAN, Y. and SHYY, W. Numerical simulations of membrane wing aerodynamics for micro air vehicle applications, *AIAA J Aircr*, July–August 2005, **42**, (4), pp 865- 873.
10. NICKEL, K. and WOHLFAHRT, M. *Tailless Aircraft in Theory and Practice*, 1994, American Institute of Aeronautics and Astronautics, Washington, DC, USA.
11. ANSYS CFX Version 12.1 Users and Theory Manuals, 2009, ANSYS.
12. ROSKAM, J. *Airplane Aerodynamics and Performance*, 1997, Design, Analysis and Research Corporation, Lawrence, KS, USA.
13. ANDERSON, J.D. *Aircraft Performance and Design*, 1999, International edition, WCB/McGraw-Hill.
14. ANDERSON, J.D. *Introduction to Flight*, 1978, McGraw-Hill, New York, USA.
15. HOAK, D.E. *et al.* USAF Stability and Control Datcom, 1978, Flight Control Division, Air Force Flight Dynamics Laboratory, Ohio, USA.
16. ROSKAM, J. *Airplane Design*, Part VI, Design, Analysis and Research Corporation, 1989, Lawrence, KS, USA.
17. PRANDTL, L. Tragflugel theorie, nachricten von der gesellschaft der wissenschaften zu Gottingen, Ges-chaeftliche Mitteilungen, Klasse, 1918, pp 451-477.
18. PRANDTL, L. Applications of modern hydrodynamics to aerodynamics, June 1921, NACA TR-116.
19. SCHILICHTING H. and TRUCKENBRADT, E. *Aerodynamics of the Airplane*, 1979, McGraw-Hill, New York, USA.
20. POPE, A. *Basic Wing and Airfoil Theory*, 1951, First edition, McGraw-Hill, New York, USA.
21. KARAMCHETI, K. *Ideal Fluid Aerodynamics*, 1966, Wiley, New York, USA.
22. KATZ, J. and PLOTKIN, A. *Low Speed Aerodynamics*, 2001, Second edition, Cambridge University Press, Cambridge, UK.
23. ANDERSON, J.D. *Fundamentals of Aerodynamics*, 2001, Third edition, McGraw-Hill, New York, USA.
24. BERTIN, J.J. *Aerodynamics for Engineers*, 2002, Fourth edition, Prentice-Hall, Upper Saddle River, NJ, USA.
25. PHILIPS, W.F. Lifting-line analysis for twisted wings and wash out optimized wings, *AIAA J Aircr*, January–February 2004, **41**, (1), pp 128-136.
26. PHILIPS, W.F., SPENCER, R.F. and SPALL, R.E. Minimizing induced drag with geometric and aerodynamic twist, CFD validation, 2005, AIAA-2005-1034, 43rd AIAA Aerospace Sciences Meeting and Exhibition, 10-13 January 2005, Reno, Nevada, USA.
27. EPPLER, R. *Airfoil Design and Data*, 1990, Springer Verlag, Berlin, Germany.
28. VANDERPLAATS, G.N. *Numerical Optimization Techniques for Engineering Design*, 1999, Vanderplaats Research and Development.
29. VANDERPLAATS, G.N. An efficient feasible directions algorithm for design synthesis, *AIAA J*, November 1984, **22,** (11), pp 633-640.
30. VisualDoc Version 6.2 Users and Theory Manuals, 2009, Vanderplaats Research and Development.
31. BECKWITH, T.G., MARANGONI, R.D. and LIENHARDV, J.H. *Mechanical Measurements*, 2007, Sixth edition, Pearson Printice Hall Education.
32. POPE, A. *Wind-Tunnel Testing*, 1954, Second edition, John Wiley & Sons.
33. FREITAS, C.J. J Fluids engineering editorial policy statement on the control of numerical accuracy, *J Fluids Eng*, 1993, **115**, pp 339-340.
34. CELIK, I., and KARATEKIN, O. Numerical experiments on application of Richardson extrapolation with nonuniform grids, *ASME J Fluid Eng*, September 1997, **119**, (3), pp 584-590.
35. MENTER, F.R., Zonal two equation k-ω turbulence models for aerodynamic flows, 1993, AIAA Paper 93-2906.
36. BARDINA, J.E., HUANG, P.G. and COAKLEY, T.J. Turbulence modeling, validation, testing and development, 1997, NASA Technical Memorandum, 110446.

https://doi.org/10.1017/S000192400000717X Published online by Cambridge University Press